HHS Public Access

Author manuscript

Comput Methods Appl Mech Eng. Author manuscript; available in PMC 2022 March 01.

Published in final edited form as:

Comput Methods Appl Mech Eng. 2021 March 1; 375: . doi:10.1016/j.cma.2020.113603.

Non-invasive Inference of Thrombus Material Properties with Physics-Informed Neural Networks

Minglang Yin[a,b], **Xiaoning Zheng**[c], **Jay D. Humphrey**[d], **George Em Karniadakis**[c,*]

[a]Center for Biomedical Engineering, Brown University, Providence, RI 02912

[b]School of Engineering, Brown University, Providence, RI 02912

[c]Division of Applied Mathematics, Brown University, Providence, RI 02912

[d]Department of Biomedical Engineering, Yale University, New Haven, CT 06520

Abstract

We employ physics-informed neural networks (PINNs) to infer properties of biological materials using synthetic data. In particular, we successfully apply PINNs on inferring permeability and viscoelastic modulus from thrombus deformation data, which can be described by the fourth-order Cahn-Hilliard and Navier-Stokes Equations. In PINNs, the partial differential equations are encoded into a loss function, where partial derivatives can be obtained through automatic differentiation (AD). In addition to tackling the challenge of calculating the fourth-order derivative in the Cahn-Hilliard equation with AD, we introduce an auxiliary network along with the main neural network to approximate the second-derivative of the energy potential term. Our model can simultaneously predict unknown material parameters and velocity, pressure, and deformation gradient fields by merely training with partial information among all data, i.e., phase field and pressure measurements, while remaining highly flexible in sampling within the spatio-temporal domain for data acquisition. We validate our model by numerical solutions from the spectral/*hp* element method (SEM) and demonstrate its robustness by training it with noisy measurements. Our results show that PINNs can infer the material properties from noisy synthetic data, and thus they have great potential for inferring these properties from experimental multi-modality and multi-fidelity data.

Keywords

Viscoelastic Porous Material; Physics-informed Neural Networks; Inverse Problem; Phase Field Model; Computational Fluids Dynamics

[*]Corresponding author: george_karniadakis@brown.edu.

Declaration of interests

The authors declare that they have no known competing financial interests or personal relationships that could have appeared to influence the work reported in this paper.

1. Introduction

Thrombus deformation and failure [38, 37] are important in deep vein thrombosis [51, 18, 17], pulmonary embolism [42, 24], and atherothrombosis [58, 8], where a key concern is thrombus failure and subsequent shedding of emboli, which can cause life-threatening complications under certain conditions. If we model a thrombus as a porous medium, where fibrin is loosely connected around the core area [52], we can study its interaction with blood flow using mathematical models, i.e., the Cahn-Hilliard and Navier-Stokes Equations [47]. Phase field modeling gives a macroscopic representation of thrombus deformation whereas the microscopic details such as the fibrin network and platelets are neglected. This system of governing equations can still reflect the mechanical interactions of a thrombus and its ambient blood flow [63, 47, 21]. Material properties, e.g., the permeability and viscoelastic modulus, in the governing equations play an important role in thrombus mechanics. Specifically, they can be indicators for the possibility of vessel occlusion and thromboembolism, since pieces of thrombus could be detached by the local shear stress and be transported to distal vessels [7]. Therefore, there is a pressing need to infer material properties from measurements, which is central to predicting thrombus shape and deformation under diverse hemodynamic conditions and assessing the risk of thromboembolism and other clinical consequences. Similar estimation of unknown parameters from data is also a central problem in electrocardiology and medical image reconstruction [23, 11, 9, 40], geophysics [29, 48, 41, 57], and many other fields [45, 53, 1, 6, 20].

However, the values of permeability and viscoelasticity are patient-specific and difficult to quantify from either experimental measurements or traditional numerical simulations using the finite element or finite volume method. A variety of numerical methods for inverse problems, i.e., Bayesian approaches [5, 56, 3], smoothing approaches [36, 19], and adjoint methods [33, 27, 31], have been developed to infer PDE parameters from data.

Recent advances in solving inverse problems using deep learning techniques provide us with a promising alternative to identify PDE parameters [30]. In particular, physics-informed neural networks (PINNs) [34, 35] is a relatively simple framework, which encodes the information from governing equations describing physical conservation laws. Specifically, the residuals of physics equations are encoded into the loss function of the neural network as constraints such that the network outputs satisfy the PDE equations as well as the initial and boundary conditions. Conceptually, adding these physical constraints restricts the optimizing weights and biases in a constrained space. Also, PINNs is a mesh-less framework since partial derivatives can be computed with automatic differentiation (AD) in most neural network packages. As a result, the residuals of PDEs can be evaluated at random points in the spatio-temporal domain for training effectively and efficiently. Additionally, for forward problems, the training data is unpaired; PINNs does not require any data other than the spatio-temporal coordinates of training points (and the initial/boundary conditions). Successful applications of PINNs range from flow visualization [35] to high-speed flows [26], stochastic PDEs [60], fractional PDEs [32], and cardiac flows [16], to name a few. For inverse problems with unknown parameters in PDEs, PINNs can infer even hundreds of parameters based only on measurements with a limited number of training points and

without any prior knowledge of the unknown parameters [35]. In PINNs, solving inverse problems follows the same workflow as forward problems only by penalizing the difference between point measurements and model predictions to the loss function. Unknown values of the parameters are set as model variables such that they can be optimized based on the gradients of the loss function with respect to their value. The potential of PINNs to infer parameters or their distributions has been explored for highly-nonlinear [34], stochastic [60], ill-posed [35, 34], multi-fidelity problems [28], non-homogeneous material properties infernce [61], and other cases [46, 4].

In this work, we apply PINNs to identify values of two parameters, namely, the permeability and viscoelastic modulus in the Cahn-Hilliard and Navier-Stokes equations. This is perhaps the first attempt to leverage the power of PINNs as a new method to infer physiological parameters using high-order multi-physics and multi-field nonlinear PDEs. In addition, to tackling the challenge of calculating the fourth-order derivative in the Cahn-Hilliard equation with AD, we introduce an auxiliary network along with the main neural network to approximate the second-derivative of the energy potential term. Moreover, we investigate the effects of the number of training points, the influence of noisy data, and different types of data on the accuracy of our inferred results.

The remainder of the paper is organized as follows: In section 2, we present the Cahn-Hilliard and Navier-Stokes system of equations as well as the PINN model. In section 3, we present the fields construction and parameter inference results for representative cases such as a thrombus and a biofilm in a channel. We also explore the sensitivity of the PINN predictions by reducing the number of training data, adding noise, and using partial data from some of the fields. We conclude in section 4 with a brief summary.

2. Methods

2.1. Cahn-Hilliard and Navier-Stokes Equations

Mechanical interaction between thrombus and blood flow as a fluid-structure interaction (FSI) problem can be modeled by the Cahn-Hilliard and phase field coupled Navier-Stokes equations (referred as Navier-Stokes equations) in fully-Eulerian coordinates [63]:

$$\rho\left(\frac{\partial \mathbf{u}}{\partial t}+\mathbf{u}\cdot\nabla\mathbf{u}\right)+\nabla p=\nabla\cdot\left(\boldsymbol{\sigma}_{vis}+\boldsymbol{\sigma}_{coh}+\boldsymbol{\sigma}_{ela}\right)-\mu\frac{(1-\phi)\mathbf{u}}{2\kappa(\phi)}, \tag{1}$$

$$\nabla\cdot\mathbf{u}=0, \tag{2}$$

$$\frac{\partial \boldsymbol{\psi}}{\partial t}+\mathbf{u}\cdot\nabla\boldsymbol{\psi}=0, \tag{3}$$

$$\frac{\partial \phi}{\partial t}+\mathbf{u}\cdot\nabla\phi=\tau\Delta\omega, \tag{4}$$

$$\omega = \Delta\phi + \gamma g(\phi), \tag{5}$$

where $\mathbf{u}(x, t)$, $p(x, t)$ $\boldsymbol{\sigma}(x, t)$, and $\phi(x, t)$ represent the velocity vector, scalar pressure, stress tensor, and scalar phase field; $g(\phi)$ equals the derivative of the double-well potential $(\phi^2 - 1)^2/4h^2$, where h is the interfacial length; $\psi = [\psi_1, \psi_2]$ denotes the auxiliary vector whose gradients are the components of the deformation gradient tensor $\mathbf{F}$ as follows:

$$\mathbf{F} := \begin{bmatrix} -\frac{\partial \psi_1}{\partial y} & -\frac{\psi_2}{\partial y} \\ \frac{\partial \psi_1}{\partial x} & \frac{\partial \psi_2}{\partial x} \end{bmatrix}.$$

Equation (1) is the Navier-Stokes equation with viscous, elastic, and cohesive stresses, respectively, which can be written as:

$$\boldsymbol{\sigma}_{vis} = \mu \nabla u, \tag{6}$$

$$\boldsymbol{\sigma}_{ela} = \nabla \cdot (\lambda_e \frac{(1-\phi)}{2}(\mathbf{F}\mathbf{F}^T - \mathbf{I})), \tag{7}$$

$$\boldsymbol{\sigma}_{coh} = \lambda \nabla \cdot (\nabla \phi \otimes \phi). \tag{8}$$

Equation (2) is the continuity equation and equation (3) denotes the transport of ψ. The fourth-order Cahn-Hilliard equation is decoupled into two second-order equations in equations (4) and (5) for formulating the weak form; γ, τ, and λ are the interfacial mobility, relaxation parameter, and mixing energy density, respectively. Note that the material parameters of interest are viscoelastic modulus λ_e and permeability $\kappa(\phi)$, which are to be determined from the data by PINNs. Other PDE parameters are assumed as known.

We impose Dirichlet boundary conditions $\mathbf{u} = g, (\mathbf{x}, t) \in \Gamma_i \times (0, T)$ for velocity at the inlet Γ_i, and no-slip boundary on the wall Γ_w. Neumann boundary conditions, i.e., $\frac{\partial \phi}{\partial \mathbf{n}} = \frac{\partial \omega}{\partial \mathbf{n}} = \frac{\partial \psi}{\partial \mathbf{n}} = 0, \mathbf{x} \in \Gamma_w \cup \Gamma_i \cup \Gamma_o$ are imposed for ψ, φ, and ω on all boundaries, and for pressure and velocity at the outlet Γ_o. This model is feasible for both 2D and 3D but we only consider two-dimensional (2D) physical domain in this paper for proof of concept demonstration.

2.2. Physics-Informed Neural Networks (PINNs)

In Fig. 1 we show a schematic of PINNs. Given the time t and coordinates x, y of training points as inputs, we construct two fully-connected neural networks, *Net U* and *Net W*, where the outputs of *Net U* represents a surrogate model for the PDE solutions u, v, p, and ϕ and the outputs of *Net W* are PDE solutions ω, ψ_1, and ψ_2. We denote the PDE solutions as $\hat{u}$ concatenated by the outputs from *Net U* and *Net W*, whose derivatives with respect to the inputs are calculated using AD. Then, we formulate the total loss L as the combination of

PDEs residual loss (L_{PDE}), initial and boundary condition loss (L_{IC}, L_{BC}), and data loss L_{data} as follows:

$$L = \omega_1 L_{PDE} + \omega_2 L_{IC} + \omega_3 L_{BC} + \omega_4 L_{data}, \tag{9}$$

and

$$L_{PDE}(\theta, \boldsymbol{\lambda}; X_{PDE}) = \frac{1}{|X_{PDE}|} \sum_{\mathbf{x} \in X_{PDE}} \left\| f(\mathbf{x}, \partial_t \hat{\mathbf{u}}, \partial_x \hat{\mathbf{u}}, \ldots, \partial_{xx} \hat{\mathbf{u}}, \ldots; \boldsymbol{\lambda}) \right\|_2^2, \tag{10}$$

$$L_{BC}(\theta, \boldsymbol{\lambda}; X_{BC}) = \frac{1}{|X_{BC}|} \sum_{\mathbf{x} \in X_{BC}} \left\| \mathfrak{B}(\hat{\mathbf{u}}, \mathbf{x}) \right\|_2^2, \tag{11}$$

$$L_{IC}(\theta, \lambda; X_{IC}) = \frac{1}{|X_{IC}|} \sum_{\mathbf{x} \in X_{IC}} \left\| \hat{\mathbf{u}} - \mathbf{u}_{t_0} \right\|_2^2, \tag{12}$$

$$L_{data}(\theta, \boldsymbol{\lambda}; X_{data}) = \frac{1}{|X_{data}|} \sum_{\mathrm{x} \in X_{data}} \left\| \hat{\mathbf{u}} - \mathbf{u}_{data} \right\|_2^2, \tag{13}$$

where ω_1, ω_2, ω_3, and ω_4 are the weights of each term. The training sets X_{PDE}, X_{BC}, and X_{IC} are sampled from the inner spatio-temporal domain, boundaries, and initial snapshot, respectively. X_{data} is the set that contains sensor coordinates and point measurements; $|\cdot|$ denotes the number of training data in the training set. In particular, $\mathfrak{B}$ represents a combination of the Dirichlet and Neumann residuals at boundaries. Finally, we optimize the model parameters $\boldsymbol{\theta}$ and the PDE parameters $\boldsymbol{\lambda} = [\lambda_e, \kappa]$ by minimizing the total loss $L(\boldsymbol{\theta}, \boldsymbol{\lambda})$ iteratively until the loss satisfies the stopping criteria. Optimizing the total loss is a searching process for $\boldsymbol{\lambda}$ such that the outputs of the PINN satisfy the PDE system, initial/boundary conditions, and point measurements. We use the mean relative L_2 error (ϵ), same as in [35], to quantify errors between reference data and model predictions:

$$\epsilon := \left(\frac{1}{N} \sum_i^N [\hat{u}(\mathbf{x}_i) - u(\mathbf{x}_i)]^2 \right) / \left(\frac{1}{N} \sum_i^N [u(\mathbf{x}_i) - \frac{1}{N} \sum_i^N u(\mathbf{x}_i)]^2 \right) \tag{14}$$

3. Results

To demonstrate the inference ability of the PINN model, we adopt four representative cases for parameters inference. The high-resolution training datasets are generated from the spectral/*hp* element solver $\mathcal{NEKTAR}$ [12] coupled with the Cahn-Hilliard equations with 3*rd*-order Jacobi polynomials. For the neural network architecture, our preliminary results suggested that using 9 hidden layers with 20 neurons per layer for *Net U* and *Net W* could be a good balance between the network representation capacity and computational costs. We use the ADAM optimizer [15] with learning rate 0.001 to train the model for a number of epochs, which is defined as the number of complete passes through the full training dataset.

The two material parameters of interest are normalized as follows. For permeability κ, we follow the normalization in [52], where $\kappa = \frac{k_f}{a_f^2}$, k_f is the true permeability and a_f is the fibrin radius. The elastic modulus λ_e of the thrombus is normalized by the magnitude of a characteristic velocity ($3.33 \times 10^{-3} m/s$) and length ($3 \times 10^{-4} m$), and it is typically of $\mathcal{O}\left(10 - 10^{-1}\right)$ with units in Pa [63, 54].

3.1. Inference of Permeability

3.1.1. Thrombus in a channel with uniform permeability—To infer the permeability κ in the Cahn-Hilliard and Navier-Stokes equations, we perform simulations for a semi-circle permeable thrombus in a channel with a steady parabolic flow coming from the left. This setup represents an idealized thrombus with an impermeable core consisting of a fibrin clot and a permeable shell region consisting of loosely-packed and partially-activated platelets. This model has been adapted as an idealized thrombus in previous works [63, 55, 59]. We impose a Neumann type boundary condition for ϕ and ψ as $\nabla\phi \cdot \mathbf{n} = \nabla\psi \cdot \mathbf{n} = 0$, where $\mathbf{n}$ is the unit vector perpendicular to the boundaries. We set the density $\rho = 1$, viscosity $\mu = 0.1$, $\lambda = 4.2428 \times 10^{-5}$, $\tau = 10^{-6}$, viscoelastic modulus $\lambda_e = 0$, and the interface length $h = 0.05$. These parameters in PINNs are non-dimensionalized values so as to be consistent with the CFD solver. The thrombus is present in the middle of the channel as shown in Fig. 2(a) with a uniform permeability in the core ($\phi = -1$) and in the outer shell layer ($\phi = 0$). In general, the inlet velocity $u(t, y)$ can be time-dependent, but in this case it is set as steady $0.3(y - 2)y$. In plot (b), we sample coordinates of training data in the initial snapshot t_0 (★), inner spatio-temporal domain from t_1 to t_n (★), and at boundaries (★). Moreover, we also sample point measurements (★) including their coordinates and PDEs solutions in the spatio-temporal domain to calculate the data loss term in the total loss. In this section, the point measurements only contain scalar data from the phase field ϕ as the data source to recover the velocity field and the value of κ. In this paper, we refer to the phase field point measurements as training data, which are randomly drawn from all points in the inner spatio-temporal domain. For each case, 1,000 points are drawn from an initial snapshot, each containing information on the phase field, velocity field, and pressure field as initial conditions. Since we want the network to satisfy the governing equations in the spatio-temporal domain and satisfy the boundary conditions, we randomly sample 25,000 inner points to compute the PDE residuals and 1,000 boundary points to compute the residuals at boundaries. Noting in particular that point measurements and inner points are drawn from the inner spatio-temporal domain, the former contains the PDE solutions whereas the latter does not. The number of inner points, initial points, and boundary points will remain the same unless specifically mentioned for all the cases in the following context.

In Fig. 3, we first show four simulation cases with permeability values from 10^{-3} to 10^{2}. We first consider a simple case with the value of κ uniform across the core and shell areas as proof of concept. We randomly sample 10,000 phase field point measurements in the spatio-temporal domain to infer κ for each case. The first column shows the reference data of phase and velocity fields at $t = 0.63$ as ground truth. As shown in Fig. 3(a), the thrombus is permeable, thus fluid can penetrate the core and shell of the thrombus. In Fig. 3(b)-(d), the fraction of fluid in the thrombus falls off dramatically as a result of a decrease of the

thrombus permeability and an accelerated area is formed on the top of the thrombus. Unlike the thrombus with large κ, fluid can hardly flow through the impermeable thrombus and the phase deformation becomes relatively small. In other words, the deformation of phase fields is noticeable when κ is large, but is minimal for permeability 0.0005. In Fig. 3, the second column depicts the predicted phase and velocity fields, and the third column shows the absolute error. The model predictions agree well with the reference data for both phase and velocity fields. The error in the phase field is mainly distributed on the thrombus interface with a maximum absolute error smaller than 10% for all cases. However, the velocity error grows with the decrease of permeability with the largest local error reaching 10% under the bottleneck region. Overall, the results show that the PINN model can regress PDE solution fields and infer parameters from synthetic data.

We summarize the results of parameter inference, mean relative L_2 errors as well as the history of inference value in Fig. 4. Plot (a) shows that all the inferred κ values fall near the diagonal line, indicating a good agreement between the reference and inferred values. Plot (b) shows the mean relative L_2 error for each case: the maximum relative error for velocity prediction is below 0.6% and for the phase field is less than 0.02%. Figs. 4 (c-f) depict the convergence history of parameter retrieval in the training process to the true different values of κ. For $\kappa = 0.5$ and 0.005, the inferred network predictions converge to the true values with 2% and 20% error. For $\kappa = 50$, the system is insensitive to the variations in κ and *a posteriori* practical identifiability analysis is provided in the Appendix. For $\kappa = 0.0005$, the velocity field has a sharp interface on the top of the thrombus surface. These reasons may lead to a discrepancy between the true and inferred value, causing a relatively large error in this special case.

To investigate the effect of the number of training points on the model prediction ability, we retrain the model for the same cases as in Fig. 3 and Fig. 4 with a different number of training points from 0.1% up to 40% of the total number of points (100,000). To clarify, the training points in Fig. 5 only include point measurements in the inner spatio-temporal domain. Figs. 5 (a, d, g, j) show the trend of the inferred values changing with the spatio-temporal resolution of the training data. Generally, the inference results converge toward the true value with mild deviations if the training data is greater than 2,500 training points (2.5% of the total number of points). The second and the third column show the mean of relative L_2 errors for velocity and phase fields. The velocity errors for κ equals 0.5 and 50 are one order smaller than those of small permeability, indicating better predictions when κ is large. The phase field errors are all lower than 1% if the training data is above 2.5% of the total number of points. Hence, for this case, we conclude that it is sufficient to guarantee convergence and good results if 2.5% of points are used to make inferences.

Furthermore, to validate the robustness of our model to noisy measurements, we add white noise $\mathcal{N}(0,1)$ to the input data, i.e., phase field ϕ, in the following way:

$$\hat{\phi} = \text{clip}(\phi + \sigma\mathcal{N}(0,1)), \hat{\phi} \in [-1, 1], \tag{15}$$

where σ is the noise level. We add normal-distributed white noise signals to the reference data ϕ and impose a clip function to restrain the value of ϕ within −1 and 1. We test the value

of the noise level σ up to 20% of the variance and train the model with these noisy data. The reference permeability value in these cases is set as 0.01. Fig. 6 (a) plots the inferred κ against various noise levels, showing that the inferred value is not affected by the added noise. In plot (b), the relative L_2 errors for phase and velocity field show slight increase as the noise level increases. In particular, the predictions of the velocity field is more sensitive to the noise as ϵ_v increases from less than 1% at $\sigma = 0$ to 25% at $\sigma = 0.20$. In general, the good agreement in parameter inference and small increment in field predictions demonstrate strong robustness of the PINN model to noisy data.

3.1.2. Thrombus in a channel with space-dependent permeability—Unlike the aforementioned idealistic case, in a real thrombus, the permeability varies spatially depending on the volume fraction (ϕ), with the core area much less permeable than the outer shell. To validate the inference ability of the PINN for a space-dependent permeability, we test another case with the $\kappa = 1$ for the shell area and $\kappa = 0.001$ for the core area as shown in Fig. 7. Since the core area is hardly permeable while the shell has a larger κ, we expect a non-uniform displacement from the thrombus core and shell as the outer layer moves with ambient flow and the inner layer stays still. To express such spatial variation explicitly, we consider a relation between ϕ and κ in this case:

$$\kappa(\phi) = e^{a\phi} + b, \tag{16}$$

where a and b are model parameters to be optimized in the PINN model and the true values of a and b are 6.90 and 0.0. Since the fluid phase ($\phi = 1$) does not have permeability, we only consider κ for the core ($\phi = -1$) and shell layer ($\phi = 0$).

In Fig. 7 we present the history of the different losses, namely PDE loss, boundary condition loss (Loss BC), initial condition loss (Loss IC), and data loss (Loss Data) in (a). Plot (b) shows the inference result for κ as a function of ϕ; the permeability at core area ($\kappa(\phi = -1) = 0.0011$) and shell area ($\kappa(\phi = 0) = 1.0003$) match the reference values well. Plot (c) shows that the model parameter quickly converges to the true values.

We present the reference data ϕ_{ref}, v_{ref} and the model predictions ϕ_{pred}, v_{pred} and their difference at $t = 0.78$ in plot (d). The field predictions exhibit a good agreement compared with the ground truth data. The errors for the phase field are mainly distributed in and around the outlet layer of the thrombus and the errors in velocity field are mainly confined within the shell layer.

3.2. Inference of viscoelastic Modulus

The viscoelastic modulus is another important parameter that has to be estimated indirectly. There are few rheometry experiments that measure the viscoelastic shear modulus λ_e with oscillatory shear deformation. We assume homogeneity and isotropy of the thrombus for simplicity. To explore the viability of parameter inference from imaging data, we consider two typical setups as illustration: a thrombus in a cavity and a biofilm in a channel.

3.2.1. Viscoelastic thrombus in a cavity—We first consider a viscoelastic thrombus in a 1×1 cavity as shown in Fig. 8 (a). This example represents a benchmark test for

simulating the deformation of a viscoelastic material. The top layer with the light gray color denotes the fluid phase while the bottom layer with the darker color indicates the initial state of the viscoelastic thrombus. We impose a time-dependent sinusoidal vertical flow $v(t, x) = -(1 - \cos(2\pi t))\sin(2\pi x)$ at the top boundary. At the left and right boundary, we set the Dirichlet boundary $\phi(y) = \tanh(y - 0.5)/\sqrt{2}h$ and the periodic boundary for velocity; we also set $\nabla\boldsymbol{\phi}\cdot\mathbf{n} = 0$ at the top boundary and $\boldsymbol{\phi} = -1$ on the bottom wall. We sample 20,000 phase field points and 2,000 pressure points at boundaries from 20 consecutive snapshots ($t \in [0.03, 0.63]$) in addition to 1,000 initial points. To train this neural network, we only utilize the phase field information and some pressure measurements at the boundaries as data sources. Such data acquisition does not require information other than the phase field from the inner spatio-temporal domain, such as the pressure or auxiliary vector field ψ, and hence it can potentially be used in a real experimental setup. The weights are chosen as followed:

$$\omega_1 = \omega_3 = 1, \omega_2 = \omega_4 = 5, \text{ epoch } \in [1, 600, 000], \tag{17}$$

$$\omega_1 = 10, \omega_3 = \omega_2 = \omega_4 = 1, \text{ epoch } \in [600, 001, 900, 000], \tag{18}$$

We set $\rho = 1$, $\mu = 0.01$, $h = 0.02$, $\lambda = 2.5 \times 10^{-9}$, and $\tau = 10^{-4}$.

In Fig. 8 we present in plot (b) the history of the loss for each term and in plot (c) the inferred value of the viscoelastic modulus. In plot (b), the PDE loss (blue line) converges around 10^{-3} and the other losses balanced at the same order with the PDE loss after redistributing the weights at epoch 600,000. Another result of changing the weights is that the inferred value for λ_e converges closer to the reference value 0.25.

Fig. 9 compares the reference data and the model predictions at time $t = 0.48$. Phase, velocity, and pressure fields are plotted respectively on each row, and the last column plots the absolute difference between the data and predictions. We can observe excellent inferred results for $\boldsymbol{\phi}$, p, and v with some minor discrepancies at the interface layer and top periodic layer. Additionally, our model renders high-resolution results in fields construction as can be seen in the summary of the mean relative L_2 error in Table 1. The first row shows the mean errors for each field over the full snapshots, while the second row lists the mean errors over the first half among all snapshots. As the data indicate, the errors increase as the system develops since the full time window errors are all greater than those at the first half time window. But overall, we can conclude that the model infers the fields for each variable with satisfactory accuracy.

3.2.2. Biofilm in a channel—In this section, we consider a thin biofilm sitting in a channel. This case is used to mimic the oscillatory shear experimental setup [63] whereas the thrombus is detached from the top surface, unlike the original setup. It is also representative for studying the mechanics of thromboembolism caused by plaque formation and rupture. Other biological implications of biofilms can be found in [47], where biofilms are aggregations embedded in a self-produced matrix of extracellular polymeric substances. From a mechanical point of view, we expect to see a different mode of oscillation on a biofilm when changing λ_e [63]. However, this effect may not be distinguishable for a semi-

circular thrombus and it will make parameter inference even more challenging. Hence, we choose the biofilm as a benchmark example.

A thin viscoelastic biofilm is present in the middle of a channel with oscillatory flow $u(t, y) = 0.9 \sin(2\pi t)(2y - y^2)$ coming from the left side of the domain. We expect to observe a swinging movement of the biofilm with the oscillatory flow. Similar to the sampling strategy on the inference of permeability, we sample the four types of points from this domain as shown in Fig. 10(b): initial points (★), inner points (★), boundary points (★), and points with measurements (★). Since the dynamics is rich in the area indicated by the black dash line, we refine the density of sampling points from t_0 to t_n within the box for better accuracy. For this 2D flow, we set $\lambda = 4.2428\times10^{-5}$, $\tau = 0.5$, $\rho = 1$, and $\mu = 0.1$, and the interface width $h = 0.04$.

In the first test, with λ_e and κ unknown, we aim to infer the parameters and recover the whole field from the training data. The model is informed with 15,000 phase field data in the spatio-temporal domain, 2,000 pressure measurements at boundaries, and 1,000 initial points. Fig. 11(a) shows the history of the training losses where the loss PDE is the largest among all losses and the loss for data measurements and initial conditions are the lowest. The inferred values for the two unknown parameters are in plot (b) and (c), indicating that the predicted λ_e and κ converge towards the actual values, at 8.27 and 0.006, as compared to the true value of $\lambda_e = 10$ and $\kappa = 0.005$. To show the regressed fields, we compare the reference data and model predictions for phase and velocity fields at times $t_0 = 0.02$, $t_1 = 0.44$, and $t_3 = 0.86$ in Fig. 12. The first column of Fig. 12 shows the actual distribution of phase and velocity fields from the reference data, and the second column shows the regressed fields from the PINN model. In plot (a), we observe overall good phase predictions in the second column with some minor smoothing effects around the sharp interface of the biofilm. Plot (b) presents the comparisons for the velocity field, and we observe that the fluid is forced to pass from the top of the biofilm, with local acceleration because of the impermeability of the biofilm. The model predictions v_{pred} show the capability of the PINN for capturing such effects and regressing the velocity field. The absolute error for the velocity field is generally below 10% with larger differences at the flow restricted area and close to the bottom boundary. We summarize the mean relative L_2 error in Table 2; the mean error for the first half time window is relatively smaller than the full time.

However, there still exists a relatively large error for inferred value of λ_e. There are three possible reasons. First, the dynamics are not very sensitive to the variation in λ_e. In the Appendix (Figure 15), we perform *a posteriori* sensitivity analysis and compared the phase and velocity field with λ_e at 15 and 0.1, demonstrating that the variation in elastic modulus mainly affects the shape and velocity around the biofilm interface. Hence, it is crucial to have an accurate prediction of the moving boundary of this fluid-structure system. Second, the interface around the biofilm is relatively sharp with rectangular corners, which poses additional difficulties in capturing the detailed but important interface dynamics. On the other hand, PINNs perform well when on inferring λ_e when the system with similar governing equations has a less sharp interface in Fig. 9. Lastly, the Cahn-Hilliard equation is essentially a fourth-order PDE system, hence, posing a challenge for neural networks to approximate such a high-order system.

Furthermore, we assess to the inference ability with different numbers and types of data. The number of training points (only includes phase field point measurements) is indicated by its ratio to the total number of points. We set κ as a known parameter to focus on the modulus λ_e. The first two rows in Fig. 13 present the inferred λ_e and mean of relative L_2 error for each field for the biofilm problem. The third and fourth rows show the same results for κ = 0.01. The inferred modulus convergences to the true value with an increasing amount of data used in training. Hence, the more training points and more data sources we use, the more accurate the results. Moreover, we shaded the 20% error region between λ_e = 8 and 12 in (a, g) which includes most of the points for yellow, black, and blue lines. By contrast, the errors in parameter inference exhibit a poor performance if only the phase field data are employed to train the neural network. Additionally, we also compare the change of the errors for each variable with the increasing number of training points in (b-f) and (h-l), and almost all points fall below or on the verge of the 5% error region shaded with gray except the training with too small training data or modality. These results demonstrate that it is sufficient to infer λ_e with a limited amount of data from the phase field and pressure measurements at the boundaries.

Finally, we investigate the inference ability on λ_e of the model to noisy measurements. We repeat a set of similar noisy tests as that in permeability inference. Results in Fig. 14 are obtained with 16,000 (8%) points measurements with the maximum noise level at 20%. The noise level is similar to that defined in equation 15 where we denote the percentage with respect to the noise variance. Fig. 14 (a) shows the inferred viscoelastic modulus at various noise levels. The inferred value is around 8 with some minor oscillations. Plot (b) illustrates that all the errors exhibit no or very little increase with the increasing intensity in noise level. Hence, we conclude that the PINN shows good robustness to noisy measurements given these findings.

4. Discussion

In this paper, we demonstrate the potential of PINNs to infer material properties of thrombus in a flow field, i.e., permeability and viscoelastic modulus, from authentic data. Such modeling leverages the recent advances in deep learning algorithms for scientific machine computing by penalizing the Cahn-Hilliard and Naiver-Stokes equations, which provides a mathematical description for thrombus deformation. Our findings agree well with permeability reference values over a wide range, i.e., from $\mathcal{O}\left(10^{-4}\right)$ to $\mathcal{O}\left(10^{1}\right)$, and the model predictions match with the simulation results from the high-order spectral/*hp* element method. In particular, only based on the phase field distribution, the PINN model inferred the value of permeability for a thrombus in a channel, suggesting a potential approach to directly estimate material properties from imaging data. For the inference of viscoelastic modulus, we show that it will be sufficient to make the inference given that the phase field data along with some pressure measurements at boundaries serve as input to the model. We also demonstrated the robustness of model inference with noisy measurements for both parameters. In addition, we successfully use PINNs to address a thrombus with a heterogeneous permeability, i.e., different permeabilities at the core and shell layer.

Phase field modeling is a special case where the concentration field can be converted from gray-scale values of the image pixels through calibration, and material properties can be directly obtained from *in operando* imaging data [62]. In our system, the multiple components and the complex geometry of a thrombus can be represented by the gray values of each pixel, which increases the possibility of using experimental images to learn thrombus properties in the future.

In this research, we have demonstrated that PINNs can regress the entire fields and unknown parameters given only partial measurements (phase field and pressure at boundaries). This provides a novel and viable way to incorporate data from imaging techniques and multi-modality data to train physics-informed deep learning models for field regression and non-invasive parameter inference in biomedical systems. A possible future improvement will be to employ instead of the governing PDEs, the Gibbs energy functional that is minimized to derive the PDEs; this may be advantageous as lower-order derivatives as well as a smaller number of equations is involved. Another future improvement will be to consider a more realistic and representative setup such as inferring parameters for a 3D thrombus with more realistic shape and unsteady ambient flow. Since predictions on the interface have a substantial impact on parameter inference, a domain decomposition based PINN model [10] can be adopted to better capture the dynamics around the interface. Also, solving such PDEs in variational form [14, 13] can help to reduce the highest order.

In terms of current limitations, one foreseeable challenge may come from the low imaging resolution, which causes difficulties to delineate and convert the presence of a shell layer with partially-activated platelet to the gray-scale values of the images. Incorrect quantification of such area can lead to a mismatch between the true and inferred value. Another possible limitation of the current study for biomedical applications is that our approach requires that the system must be represented via explicit governing differential equations, whereas the governing equations for many biological processes are not known a priori. Promising remedies to overcome such challenge are data-driven system identification [2, 25, 39, 43], or variational system identification [49, 50] for discovering hidden governing equations from noisy and sparse data. Also, high dimensionality and lack of boundary/initial information could deteriorate the overall accuracy of the model predictions.

In ongoing work, we are extending our research by exploring the possibility of using imperfect PDE constraints and also noise-filtering techniques for realistic imaging data. Furthermore, although PINNs are less data-hungry compared to traditional data-driven models, the amount of data used in training, from an experimental point of view, is still quite intensive given the small dimensions and limited spatio-temporal resolution of imaging. In particular, the inference of biomechanical properties of a realistic thrombus depend on its internal properties, topology, and ambient flow (possibly surrounded by turbulent flow [44]), which requires considerable data to fully capture such dependencies. *In vivo* or *in vitro* experimental data combining multi-modality imaging techniques, such as ultrasound (US) and optical coherence tomography (OCT), or panoramic-digital imaging correlation (pDIC), can accurately reflect the real vessel geometries and material properties. However, the morphological diversity of a thrombus and expensive experimental cost make acquiring sufficient experimental data impractical. Multi-fidelity frameworks [22, 28], leveraging data

from different modalities, seem to be promising for addressing these issues given the insufficient amount of high fidelity data. Specifically, the high fidelity data can be realistic, but expensive experimental imaging data with actual material properties (i.e., viscoelastic modulus and permeability). On the other hand, considerable low-fidelity *in silico* data represented by computational results from finite-element simulations can be generated. The multi-fidelity machine-learning framework can learn to optimally combine the multi-modality experimental data with simulations to obtain a response surface for the biomechanical properties of a thrombus in response to the morphological and physiological variables. We are currently working on extending this multi-fidelity/multimodality framework, and we will report our results in a future publication.

Acknowledgment

The work is supported by grant U01 HL142518 National Institute of Health.

Appendix

A4. A posteriori practical identifiability analysis for κ and λe

We perform *a posteriori* sensitivity analysis to κ in Fig. 15. We rerun a set of simulations for a thrombus in a channel with $\kappa = 50 - 0.0005$ and plot the phase field difference when κ is set as the true value and inferred value. In (a) the maximum difference in the phase field for $\kappa = 50$ is at 2.5×10^{-5} while the maximum difference for $\kappa = 0.0005$ is almost 1,000 times larger, showing that the system is relatively insensitive to variations in κ when permeability is large. Therefore, the system is less "sensitive" when $\kappa = 50$ than κ is at $\mathcal{O}\left(1 - 10^{-4}\right)$ and it is harder to have an accurate inference results when $\kappa = 50$.

In Fig. 16 we present fields comparison when $\lambda_e = 0.1$ and 15 for the biofilm problem. In Fig. 16 (a), we observe small differences between the deformation of the biofilm at the same time where most of the differences appear at the interface. Plot (b) compares the velocity field where we observe an acceleration area on the top of the biofilm. However, the main inconsistency is caused by the velocity inside the biofilm. In plot (c) we show the pressure field comparison and we observe an overall similar pressure distribution for λ_e at different values with minor differences close to the center. Overall, the results in Fig. 16 and 15 demonstrate that the parameter sensitivity for κ and λ_e pose a difficulty on the inverse inference to the unknown parameters.

A2. Supplementary results for the inference of λe

In this section, we present two more additional tests result from the network trained with $\phi + u$ (green line) and $u + p$ (purple line) in Fig. 17 on the top of Fig. 13. The inferred parameter value on the purple line has the largest error among all lines, and the phase field error ended at the order of 1, indicating converged training results from the PINN model by only using information from velocity and pressure fields. The green line shows the results from training with ϕ and u. While the error in (e-i) shows a satisfactory agreement with the actual data, the inferred parameter value still cannot match the true value very well. We use these two tests as a supplementary proof to show the importance of pressure data on the inference of λ_e.

A3. Inferring permeability from a pre-trained model

In this section, we briefly discuss the possibility to infer parameter values from a pre-trained model. To be more specific, we use the weights and biases of a network for inferring $\kappa = 0.5$ as the initial state to infer $\kappa = 0.005$ and 0.0005. Figure 18 plots the value of κ and total loss against training epochs for PINNs with a pre-trained model and randomized initialization. For $\kappa = 0.005$, (a) and (b) show that the model with pre-training shows a faster convergence on inferring κ and minimizing loss compared with the model without pre-training. However, pre-training may not be helpful for impermeable thrombus ($\kappa = 0.0005$) even if the initialization of κ is far from the true value. So the effect of using a pre-trained model as initialization for faster convergence is case dependent and needs a more detailed and careful discussion in our future work.

A4. Relative L2 error over time

In this section, we plot the relative L_2 error over time for the cavity and biofilm example. The errors in the first half window are smaller than that in the full time window. The relative errors in every field increase over time, hence suggesting that longer time integration may cause larger deviations on the field predictions.

References

[1]. Bishwal JP Parameter estimation in stochastic differential equations (Springer, 2007).

[2]. Brunton SL, Proctor JL, and Kutz JN. Discovering governing equations from data by sparse identification of nonlinear dynamical systems. Proceedings of the national academy of sciences 113:3932–3937, 2016.

[3]. Calderhead B, Girolami M, and Lawrence ND. Accelerating bayesian inference over nonlinear differential equations with gaussian processes. In: Advances in neural information processing systems, pp. 217–224 (2009).

[4]. Chen Y, Lu L, Karniadakis GE, and Dal Negro L. Physics-informed neural networks for inverse problems in nano-optics and metamaterials. Optics Express 28:11618–11633, 2020. [PubMed: 32403669]

[5]. Chkrebtii OA, Campbell DA, Calderhead B, Girolami MA et al. Bayesian solution uncertainty quantification for differential equations. Bayesian Analysis 11:1239–1267, 2016.

[6]. Crassidis JL and Junkins JL. Optimal estimation of dynamic systems (CRC press, 2011).

[7]. Di Nisio M, van Es N, and Büller HR. Deep vein thrombosis and pulmonary embolism. The Lancet 388:3060–3073, 2016.

[8]. Endo S, Kuwayama N, Hirashima Y, Akai T, Nishijima M, and Takaku A. Results of urgent thrombolysis in patients with major stroke and atherothrombotic occlusion of the cervical internal carotid artery. American Journal of Neuroradiology 19:1169–1175, 1998. [PubMed: 9672034]

[9]. Hamilton SJ and Hauptmann A. Deep d-bar: Real-time electrical impedance tomography imaging with deep neural networks. IEEE transactions on medical imaging 37:2367–2377, 2018. [PubMed: 29994023]

[10]. Jagtap AD, Kharazmi E, and Karniadakis GE. Conservative physics-informed neural networks on discrete domains for conservation laws: Applications to forward and inverse problems. Computer Methods in Applied Mechanics and Engineering 365:113028, 2020.

[11]. Jin KH, McCann MT, Froustey E, and Unser M. Deep convolutional neural network for inverse problems in imaging. IEEE Transactions on Image Processing 26:4509–4522, 2017. [PubMed: 28641250]

[12]. Karniadakis G and Sherwin S. Spectral/hp element methods for computational fluid dynamics (Oxford University Press, 2013).

[13]. Kharazmi E, Zhang Z, and Karniadakis GE. Variational physics-informed neural networks for solving partial differential equations. arXiv preprint arXiv:1912.00873, 2019.

[14]. Kharazmi E, Zhang Z, and Karniadakis GE. hp-vpinns: Variational physics-informed neural networks with domain decomposition. arXiv preprint arXiv:2003.05385, 2020.

[15]. Kingma DP and Ba J. Adam: A method for stochastic optimization. arXiv preprint arXiv:1412.6980, 2014.

[16]. Kissas G, Yang Y, Hwuang E, Witschey WR, Detre JA, and Perdikaris P. Machine learning in cardiovascular flows modeling: Predicting arterial blood pressure from non-invasive 4d flow mri data using physics-informed neural networks. Computer Methods in Applied Mechanics and Engineering 358:112623, 2020.

[17]. Kyrle PA and Eichinger S. Deep vein thrombosis. The Lancet 365:1163–1174, 2005.

[18]. Lensing AW, Prandoni P, Prins MH, and Büller H. Deep-vein thrombosis. The Lancet 353:479–485, 1999.

[19]. Liang H and Wu H. Parameter estimation for differential equation models using a framework of measurement error in regression models. Journal of the American Statistical Association 103:1570–1583, 2008. [PubMed: 19956350]

[20]. Lieberman C and Willcox K. Goal-oriented inference: Approach, linear theory, and application to advection diffusion. SIAM Review 55:493–519, 2013.

[21]. Lin F-H, Liu C, and Zhang P. On hydrodynamics of viscoelastic fluids. Communications on Pure and Applied Mathematics 58:1437–1471, 2005.

[22]. Lu L, Dao M, Kumar P, Ramamurty U, Karniadakis GE, and Suresh S. Extraction of mechanical properties of materials through deep learning from instrumented indentation. Proceedings of the National Academy of Sciences 117:7052–7062, 2020.

[23]. Lucas A, Iliadis M, Molina R, and Katsaggelos AK. Using deep neural networks for inverse problems in imaging: beyond analytical methods. IEEE Signal Processing Magazine 35:20–36, 2018.

[24]. Mammen EF Pathogenesis of venous thrombosis. Chest 102:640S–644S, 1992. [PubMed: 1451539]

[25]. Mangan NM, Brunton SL, Proctor JL, and Kutz JN. Inferring biological networks by sparse identification of nonlinear dynamics. IEEE Transactions on Molecular, Biological and Multi-Scale Communications 2:52–63, 2016.

[26]. Mao Z, Jagtap AD, and Karniadakis GE. Physics-informed neural networks for high-speed flows. Computer Methods in Applied Mechanics and Engineering 360:112789, 2020.

[27]. Maute K, Nikbay M, and Farhat C. Sensitivity analysis and design optimization of three-dimensional non-linear aeroelastic systems by the adjoint method. International Journal for Numerical Methods in Engineering 56:911–933, 2003.

[28]. Meng X and Karniadakis GE. A composite neural network that learns from multi-fidelity data: Application to function approximation and inverse pde problems. Journal of Computational Physics 401:109020, 2020.

[29]. Menke W Geophysical data analysis: Discrete inverse theory (Academic press, 2018).

[30]. Michoski C, Milosavljevic M, Oliver T, and Hatch D. Solving irregular and data-enriched differential equations using deep neural networks. arXiv preprint arXiv:1905.04351, 2019.

[31]. Nguyen VT, Georges D, and Besançon G. State and parameter estimation in 1-d hyperbolic pdes based on an adjoint method. Automatica 67:185–191, 2016.

[32]. Pang G, Lu L, and Karniadakis GE. fpinns: Fractional physics-informed neural networks. SIAM Journal on Scientific Computing 41:A2603–A2626, 2019.

[33]. Piasecki M and Katopodes ND. Identification of stream dispersion coefficients by adjoint sensitivity method. Journal of Hydraulic Engineering 125:714–724, 1999.

[34]. Raissi M, Perdikaris P, and Karniadakis GE. Physics-informed neural networks: A deep learning framework for solving forward and inverse problems involving nonlinear partial differential equations. Journal of Computational Physics 378:686–707, 2019.

[35]. Raissi M, Yazdani A, and Karniadakis GE. Hidden fluid mechanics: Learning velocity and pressure fields from flow visualizations. Science 367:1026–1030, 2020. [PubMed: 32001523]

[36]. Ramsay JO, Hooker G, Campbell D, and Cao J. Parameter estimation for differential equations: a generalized smoothing approach. Journal of the Royal Statistical Society: Series B (Statistical Methodology) 69:741–796, 2007.

[37]. Rausch MK and Humphrey JD. A microstructurally inspired damage model for early venous thrombus. Journal of the mechanical behavior of biomedical materials 55:12–20, 2016.

[38]. Rausch MK and Humphrey JD. A computational model of the biochemomechanics of an evolving occlusive thrombus. Journal of Elasticity 129:125–144, 2017.

[39]. Rudy SH, Brunton SL, Proctor JL, and Kutz JN. Data-driven discovery of partial differential equations. Science Advances 3:e1602614, 2017. [PubMed: 28508044]

[40]. Rudy Y and Oster H. The electrocardiographic inverse problem. Critical reviews in biomedical engineering 20:25–45, 1992. [PubMed: 1424685]

[41]. Sambridge M Geophysical inversion with a neighbourhood algorithm-i. searching a parameter space. Geophysical journal international 138:479–494, 1999.

[42]. Sevitt S and Gallagher N. Venous thrombosis and pulmonary embolism. a clinico-pathological study in injured and burned patients. British Journal of Surgery 48:475–489, 1961.

[43]. Shea DE, Brunton SL, and Kutz N. Sindy-bvp: Sparse identification of nonlinear dynamics for boundary value problems. arXiv preprint arXiv:2005.10756, 2020.

[44]. Smith RL, Blick EF, Coalson J, and Stein PD. Thrombus production by turbulence. Journal of applied physiology 32:261–264, 1972. [PubMed: 5007881]

[45]. Tahmasebi P, Javadpour F, and Sahimi M. Stochastic shale permeability matching: Three-dimensional characterization and modeling. International Journal of Coal Geology 165:231–242, 2016.

[46]. Tartakovsky AM, Marrero CO, Perdikaris P, Tartakovsky GD, and Barajas-Solano D. Learning parameters and constitutive relationships with physics informed deep neural networks. arXiv preprint arXiv:180803398, 2018.

[47]. Tierra G, Pavissich JP, Nerenberg R, Xu Z, and Alber MS. Multicomponent model of deformation and detachment of a biofilm under fluid flow. Journal of The Royal Society Interface 12:20150045, 2015.

[48]. Treitel S and Lines L. Past, present, and future of geophysical inversiona new millennium analysis. Geophysics (66):21–24, 2001.

[49]. Wang Z, Huan X, and Garikipati K. Variational system identification of the partial differential equations governing the physics of pattern-formation: inference under varying fidelity and noise. Computer Methods in Applied Mechanics and Engineering 356:44–74, 2019.

[50]. Wang Z, Huan X, and Garikipati K. Identification of the partial differential equations governing microstructure evolution in materials: Inference over incomplete, sparse and spatially non-overlapping data. arXiv preprint arXiv:2001.04816, 2020.

[51]. Weinmann EE and Salzman EW. Deep-vein thrombosis. New England Journal of Medicine 331:1630–1641, 1994.

[52]. Wufsus A, Macera N, and Neeves K. The hydraulic permeability of blood clots as a function of fibrin and platelet density. Biophysical journal 104:1812–1823, 2013. [PubMed: 23601328]

[53]. Wunsch C The ocean circulation inverse problem (Cambridge University Press, 1996).

[54]. Xu S, Xu Z, Kim OV, Litvinov RI, Weisel JW, and Alber M. Model predictions of deformation, embolization and permeability of partially obstructive blood clots under variable shear flow. Journal of the Royal Society Interface 14:20170441, 2017.

[55]. Xu Z, Chen N, Kamocka MM, Rosen ED, and Alber M. A multiscale model of thrombus development. Journal of the Royal Society Interface 5:705–722, 2008.

[56]. Xun X, Cao J, Mallick B, Maity A, and Carroll RJ. Parameter estimation of partial differential equation models. Journal of the American Statistical Association 108:1009–1020, 2013.

[57]. Yang Y, Engquist B, Sun J, and Hamfeldt BF. Application of optimal transport and the quadratic wasserstein metric to full-waveform inversion. Geophysics 83:R43–R62, 2018.

[58]. Yasaka M, Yamaguchi T, and Shichiri M. Distribution of atherosclerosis and risk factors in atherothrombotic occlusion. Stroke 24:206–211, 1993. [PubMed: 8421820]

[59]. Yazdani A, Li H, Humphrey JD, and Karniadakis GE. A general shear-dependent model for thrombus formation. PLoS computational biology 13:e1005291, 2017. [PubMed: 28095402]

[60]. Zhang D, Lu L, Guo L, and Karniadakis GE. Quantifying total uncertainty in physics-informed neural networks for solving forward and inverse stochastic problems. Journal of Computational Physics 397:108850, 2019.

[61]. Zhang E, Yin M, and Karniadakis GE. Physics-informed neural networks for nonhomogeneous material identification in elasticity imaging. arXiv preprint arXiv:2009.04525, 2020.

[62]. Zhao H, Storey BD, Braatz RD, and Bazant MZ. Learning the physics of pattern formation from images. Physical Review Letters 124:060201, 2020. [PubMed: 32109085]

[63]. Zheng X, Yazdani A, Li H, Humphrey JD, and Karniadakis GE. A three-dimensional phase-field model for multiscale modeling of thrombus biomechanics in blood vessels. PLOS Computational Biology 16:e1007709, 2020. [PubMed: 32343724]

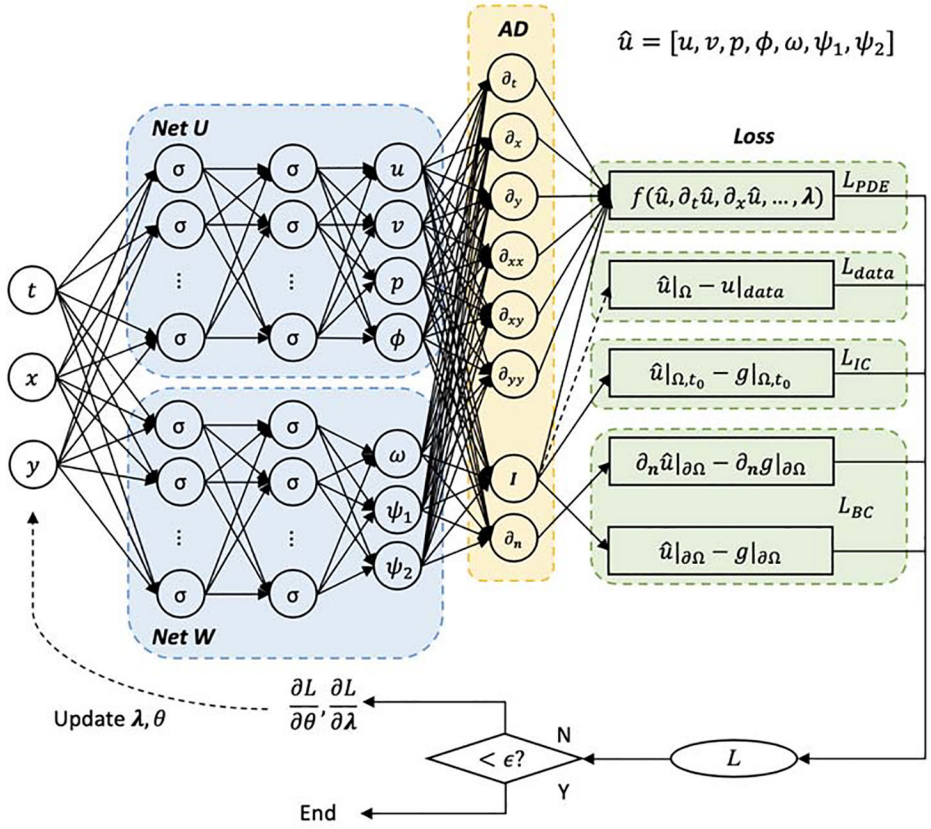

Figure 1: Schematic of a PINN for solving inverse problem for Cahn-Hilliard and Navier-Stokes PDEs.

Circled by blue boxes, *Net U* and *Net W* represent surrogate models for the PDEs solution whose derivatives can be computed with automatic differentiation (AD). The computed derivatives are used in the loss function to restrict model outputs such that they satisfy the system of PDEs in Ω. For inverse problems, the residual between sensor measurements $u|_{\text{data}}$ and model outputs $\hat{u}_\Omega$ are included in the loss function. We use ADAM to optimize the model parameters $\boldsymbol{\theta}$ (weights and biases) and search the unknown values of the material parameters from the PDEs $\boldsymbol{\lambda}$ to minimize the loss function.

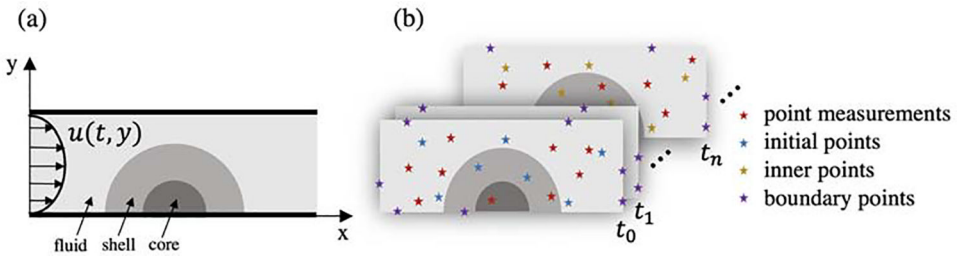

Figure 2: 2D flow past a thrombus.

(a) The computational domain is a channel with walls on the top and bottom boundaries with the inlet flow $u(t, y)$ entering from the left side.; ϕ=1 corresponds to fluid. A thrombus with a permeable core $\phi = -1$ and shell $\phi = 0$ is present at the bottom boundary. (b) Sampling points for inferring permeability include initial points (★) at the time t_0, inner points (★) from t_1 to t_n, boundary points (★) on boundaries, and point measurements (★) with PDE solutions.

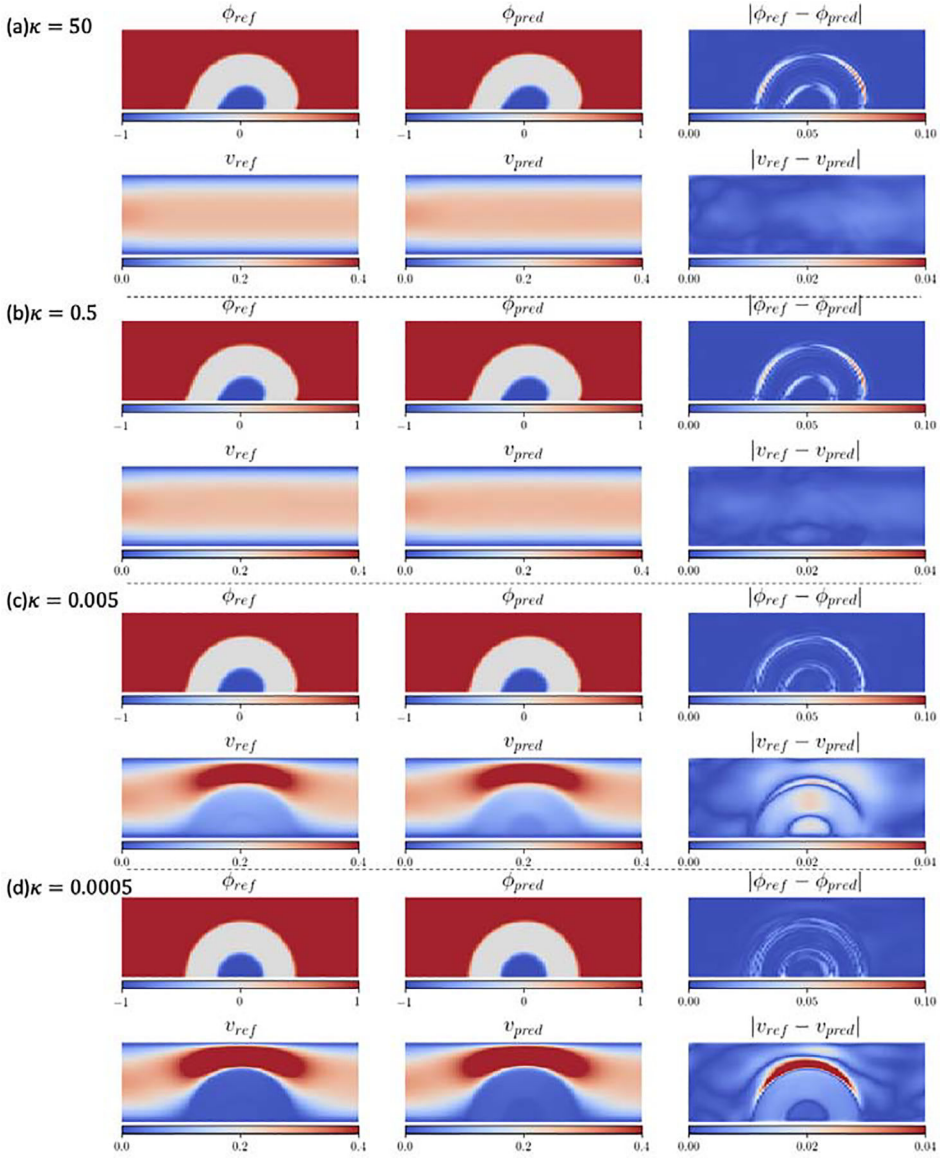

Figure 3: Prediction and error of 2D flow past a thrombus for various permeability values at *t* = 0.63.

Representative snapshots of the reference data for permeability value κ (a) 50 (b) 0.5 (c) 0.005 (d) 0.0005 are shown against the predicted phase and velocity field. The first column shows the reference simulation results while the second shows the results from the PINNs. The third column shows the absolute value of the difference between references and model predictions. The network is informed by 10,000 point measurements drawn from $t \in [0.33, 0.63]$.

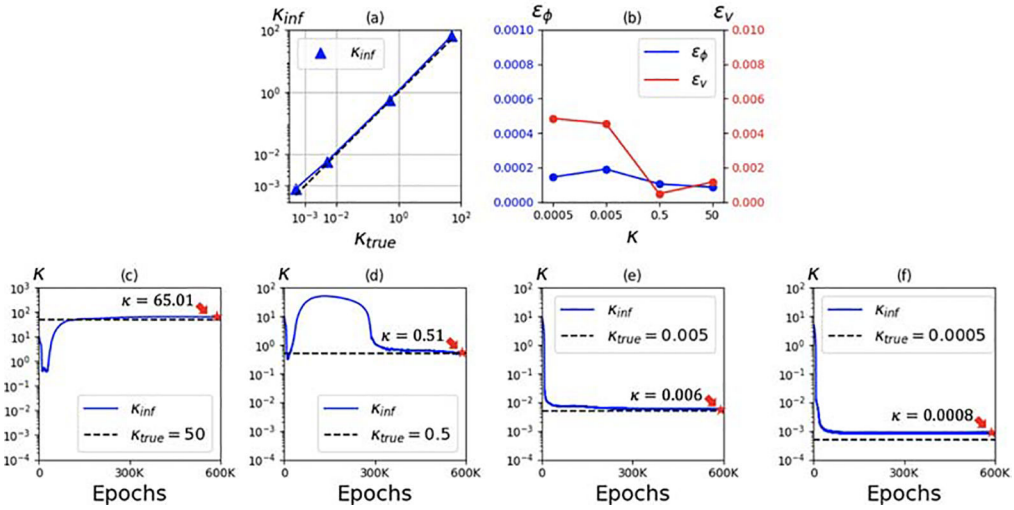

Figure 4: Performance and history of PINN on predicting permeability of 2D flow past a thrombus with κ ranging from 0.0005 to 50.

(a) Comparison of the inferred values with the reference values. (b) Mean relative L_2 errors for phase and velocity field when κ varies from 0.0005 to 50. The plots in (c, d, e, f) illustrate the inference of the permeability with respect to the number of iterations of PINN when $\kappa = 50$, $\kappa = 0.5$, $\kappa = 0.005$, and $\kappa = 0.0005$. The number of training points is 10,000.

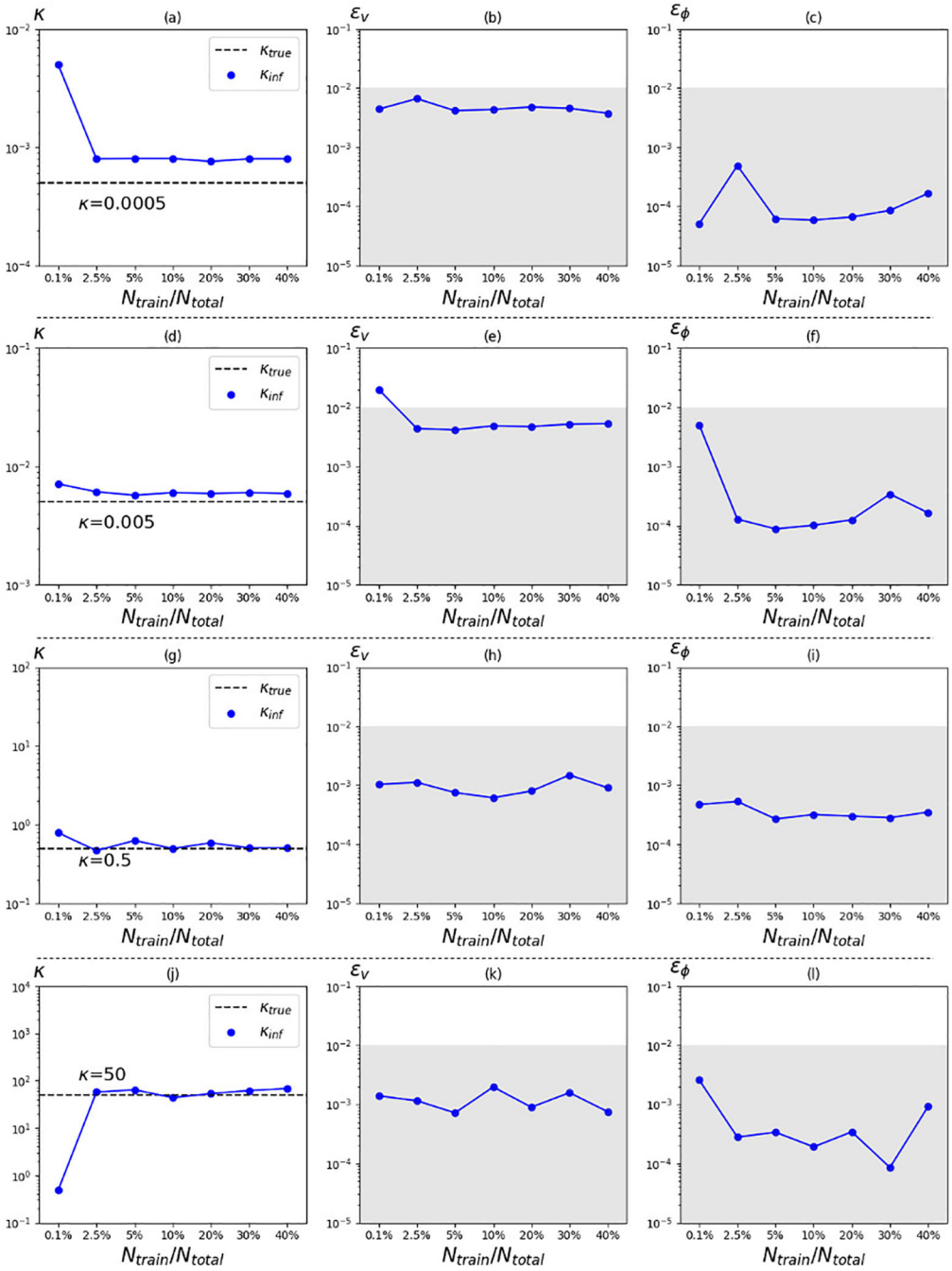

Figure 5: Effect of the number of training points on the accuracy of PINNs.

N_{total} = 100,000. Plots (a, d, g, j) show comparison of reference and inferred permeability for a different number of training points from 0.1% of the total number of points to 40%. The second and the third column show the mean of relative L_2 error for (b, e, h, k) velocity field and (c, f, i, l) phase field over time for different numbers of training points. We shaded the area where the error is lower than 1%.

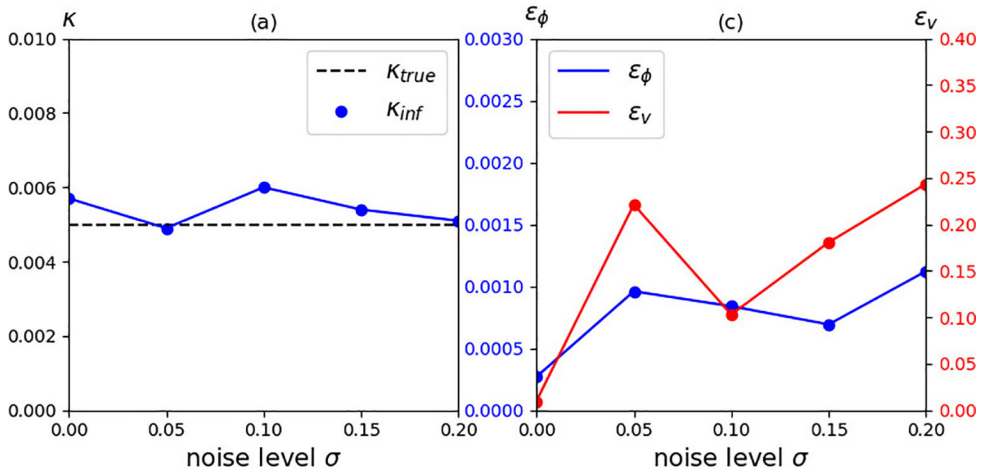

Figure 6: Predictions of 2D flow past a thrombus trained with noisy phase field measurements.

(a) Inferred permeability and (c) mean relative L_2 errors between the model predictions and the reference for phase ϵ_ϕ and velocity field ϵ_v. Noise is added to the phase field with the noise level ranged from 0 to 20%. Here, 10,000 data points are scattered in the spatio-temporal domain as the training data to infer the permeability.

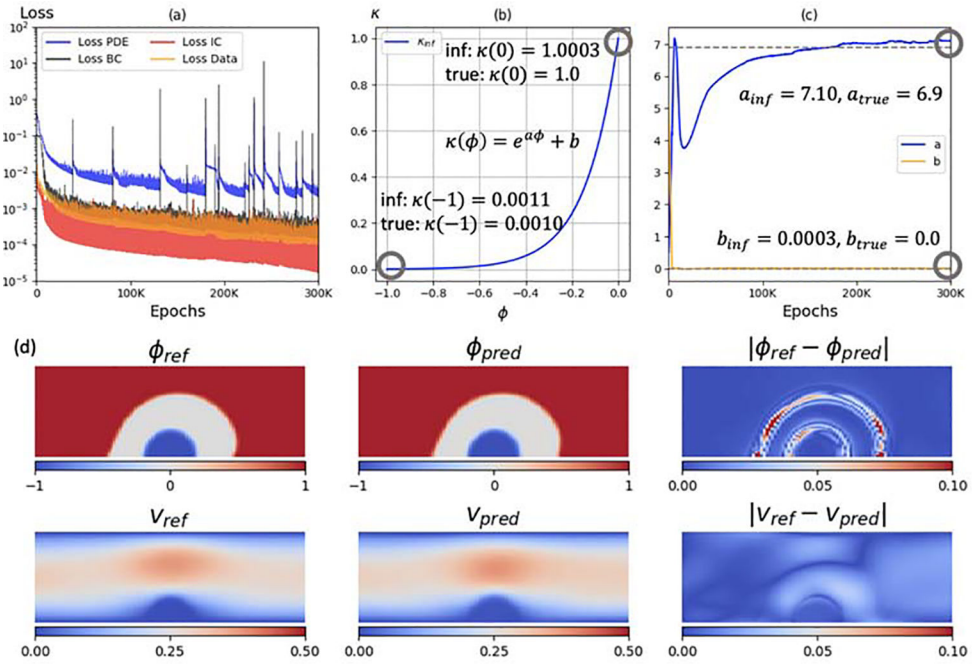

Figure 7: 2D flow past a thrombus with phase dependent permeability.

(a) History of network losses (Loss PDE, Loss IC, Loss BC, and Loss Data) and (b) inferred the permeability κ as a function of ϕ. (c) The values of a and b at each epoch. (d) Comparison of phase field and velocity field for $\kappa(\phi)$ at $t = 0.78$ and their absolute error. The core permeability is 0.001 and the shell permeability is set 1 as the actual values. 10,000 data points are scattered in the spatio-temporal domain from 30 snapshots ($t \in [0.03, 0.93]$) as the training data to infer the permeability.

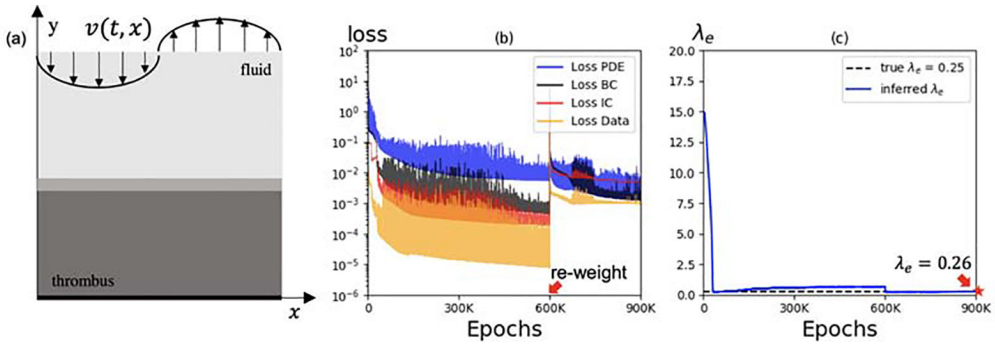

Figure 8: (a) Schematic for viscoelastic thrombus in a cavity, (b) history losses for each term, and (c) inference of λ_e.

(a) We impose a time-dependent sinusoidal vertical velocity $v(t, x) = -(1 - \cos(2\pi t))$ $\sin(2\pi x)$ at the top boundary, and set the left and right sides as periodic. We changed the weight for each loss term at epoch 600,000. Training data points are scattered among the spatio-temporal domain to train the network, including 20,000 phase field points from the inner spatio-temporal domain, 2,000 pressure measurements at boundaries, and 1,000 initial points. Loss PDE: loss for the PDEs residuals, Loss BC: loss for boundary conditions, Loss IC: loss for initial conditions, Loss Data: loss for measurements data.

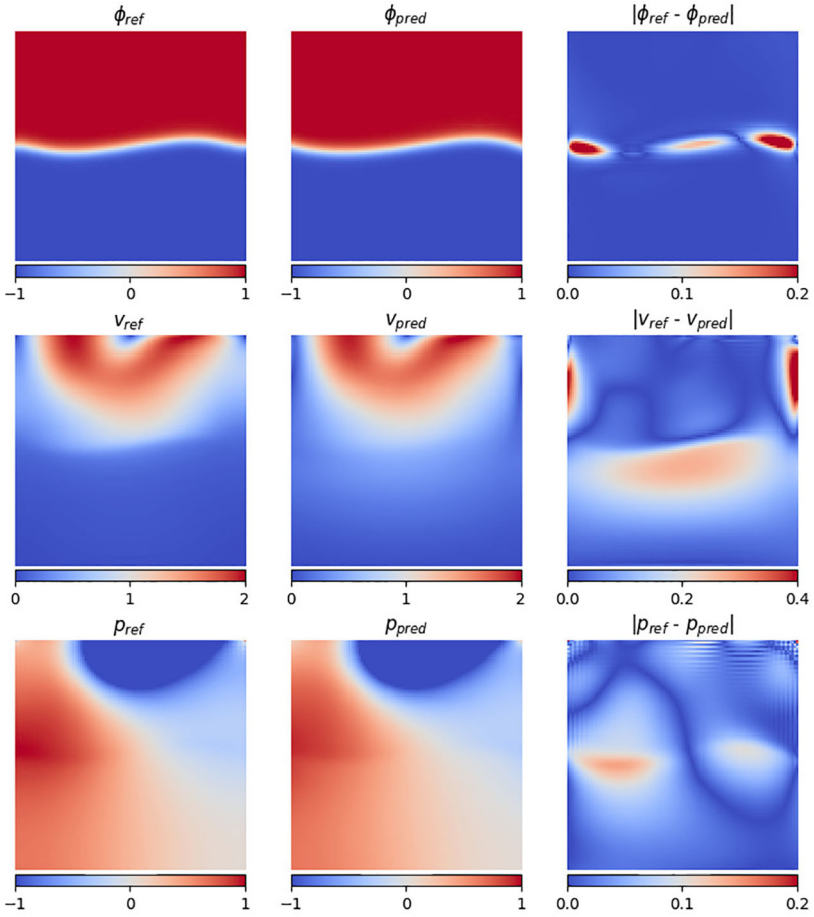

Figure 9: Viscoelastic thrombus in a cavity.

The first column presents the phase field distribution ϕ, velocity field v, and pressure distribution p from reference data, respectively. The second column shows the same field predictions from the model at $t = 0.48$. The absolute difference between the data and the model predictions are plotted in the third column.

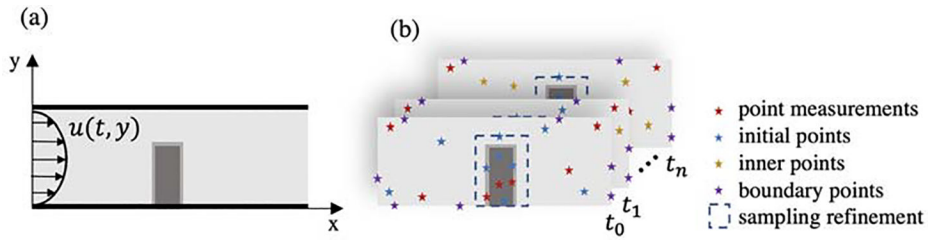

Figure 10: 2D flow past a viscoelastic biofilm setup.

(a) The computational domain is a channel with wall boundaries on the top and bottom sides, and with flow $u(t)$ entering from the left side. A viscoelastic biofilm is present at the bottom boundary. (b) Training points include initial points (★) at time t_0, inner points (★) from t_1 to t_n, boundary points (★) on the boundaries, and point measurements (★) with PDE solutions. The sampling points are refined within the dashed line area to improve the results of the PINN model.

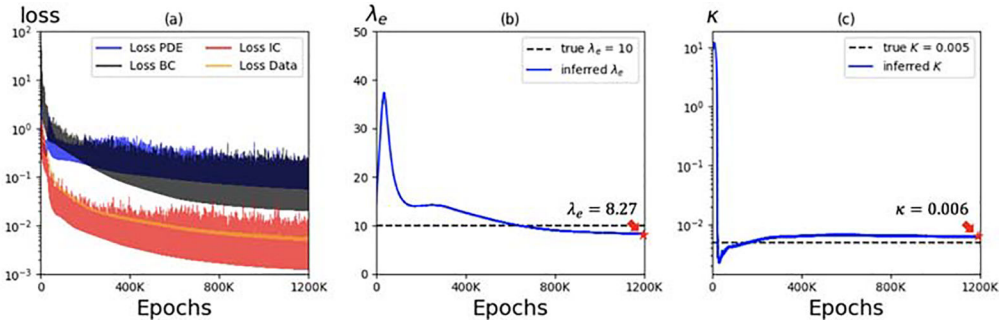

Figure 11: History of (a) network losses and inference for (b, c) λ_e and κ against the number of training epochs for the biofilm problem.

The full time window is from 0.02 to 1.16.

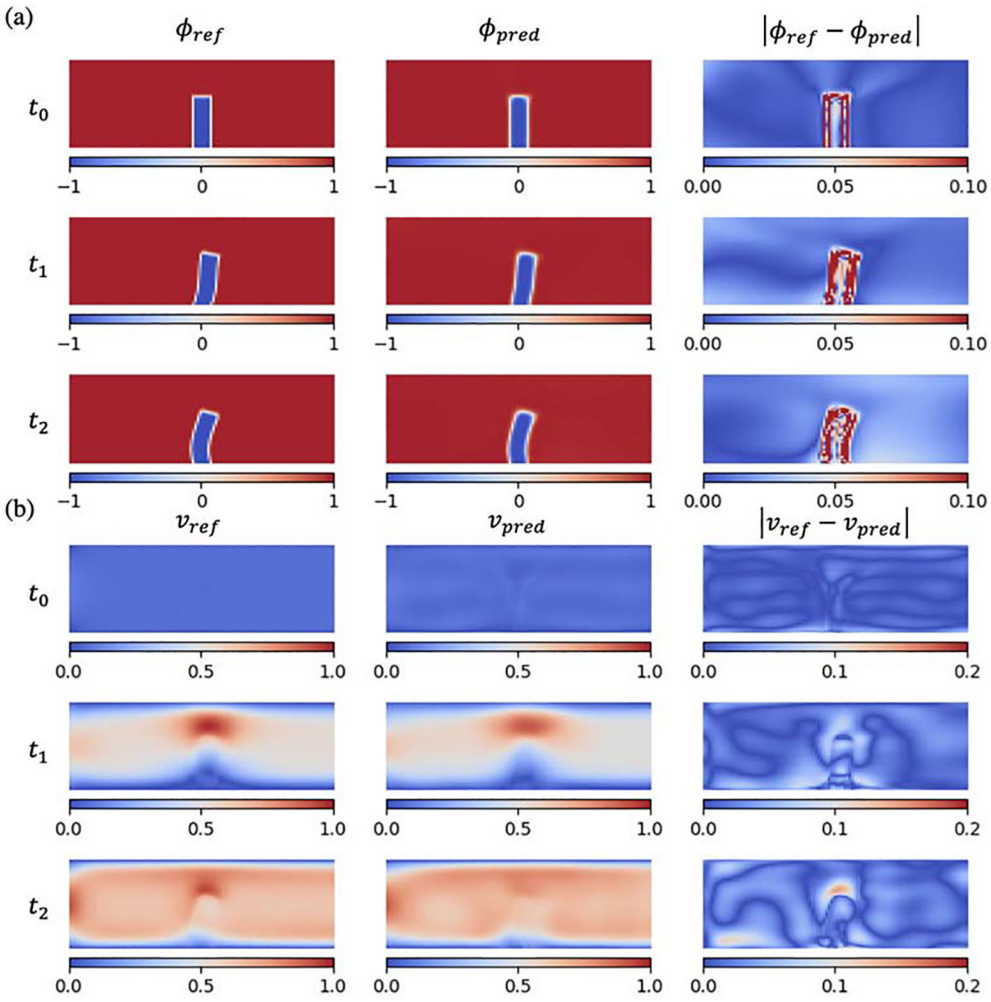

Figure 12: 2D flow past a viscoelastic biofilm.

With λ_e and κ unknown at the same time, we sample 15,000 phase field data, 2,000 pressure points at boundaries, and 1,000 initial points as the training data for parameters inference and field regression. The time is from 0.02 to 1.16. Representative snapshots (at $t_0 = 0.02$, $t_1 = 0.44$, and $t_2 = 0.86$) of the reference (a) phase field and (b) velocity fields are shown against the predicted phase and velocity from the model. The first column shows the reference fields from simulation, the second shows the predicted results from PINNs, and the third column shows the absolute value of the difference between the references and the model predictions.

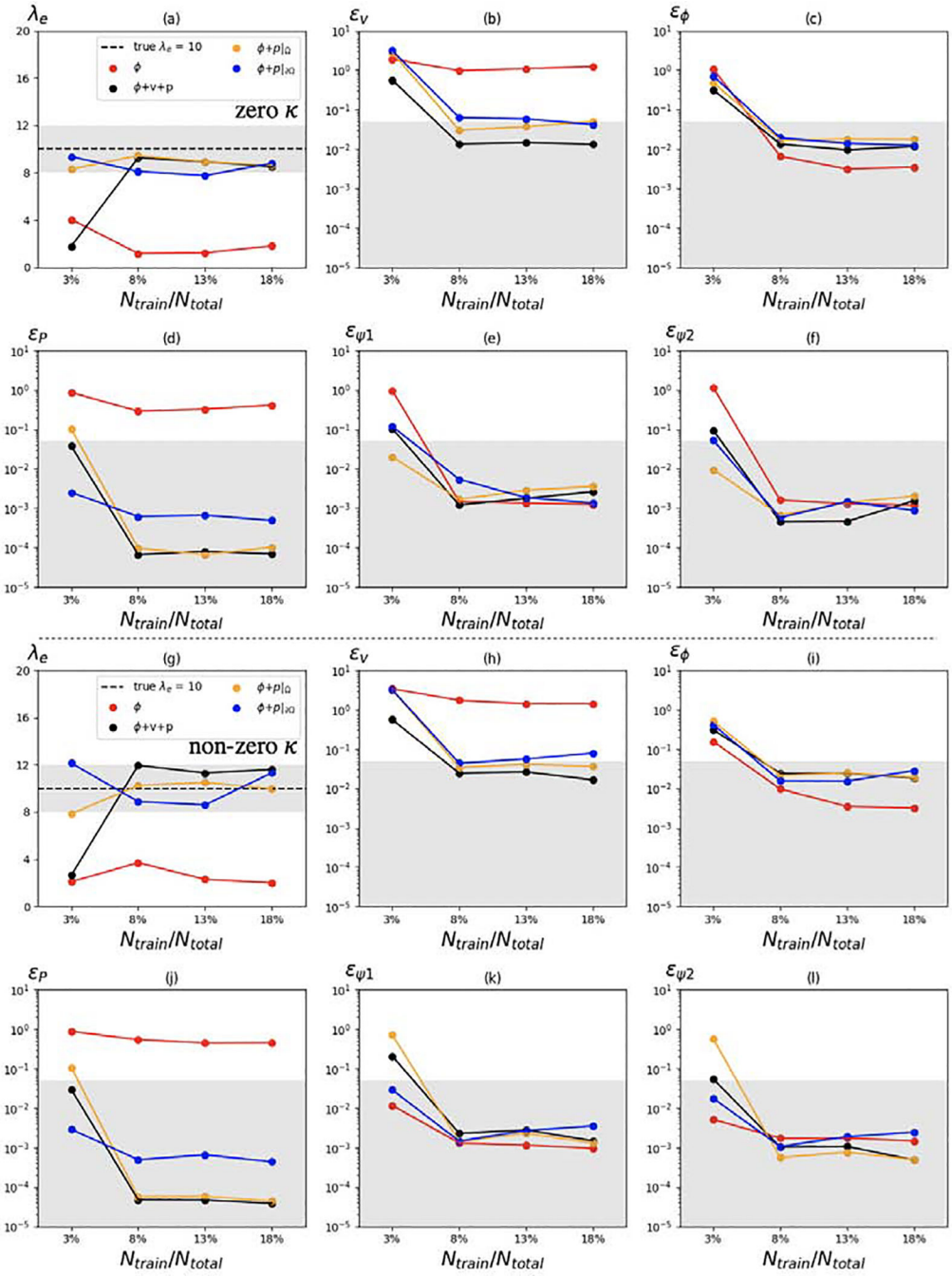

Figure 13: Effect of the number of training points on the prediction value of λ_e with κ value as known.

(a, g) Predicted λ_e versus the number of training points for case with zero κ and non-zero κ. (b-f, h-l) The mean relative error L_2 versus the number of training points for each field when $\kappa = 10$ and $\kappa = 0.01$. We also plotted the inference results and L_2 error given various training data sources such as ϕ+u+p, ϕ+p, and only with ϕ. For the one with pressure information and phase field, inner (Ω) and boundary (∂) pressure measurements are used respectively to train the neural network. We shaded areas with lower than 5% of error. $t \in [0.02,1.16]$, $N_{total} =$ 200,000.

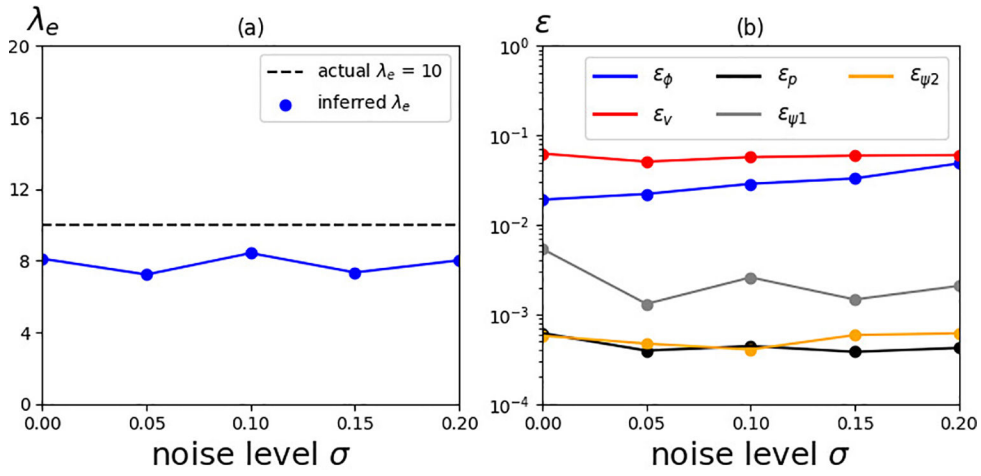

Figure 14: 2D flow past a viscoelastic biofilm trained with noisy measurements with λ_e unknown.

(a) The inferred λ_e. (b) presents the mean relative L_2 errors between the model predictions and the references for each field. Noise is added to the phase field with the noise level ranged from 0 to 20%. Here, 16,000 (8%) data points are scattered in the spatio-temporal domain.

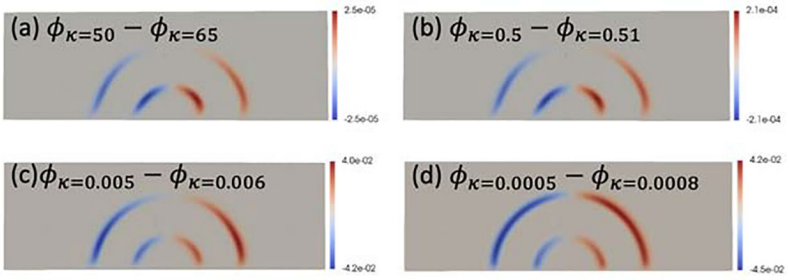

Figure 15: *A posteriori* practical identifiability analysis of κ to the phase field.
(a-d) Phase field difference between κ is set as true values and inferred values.

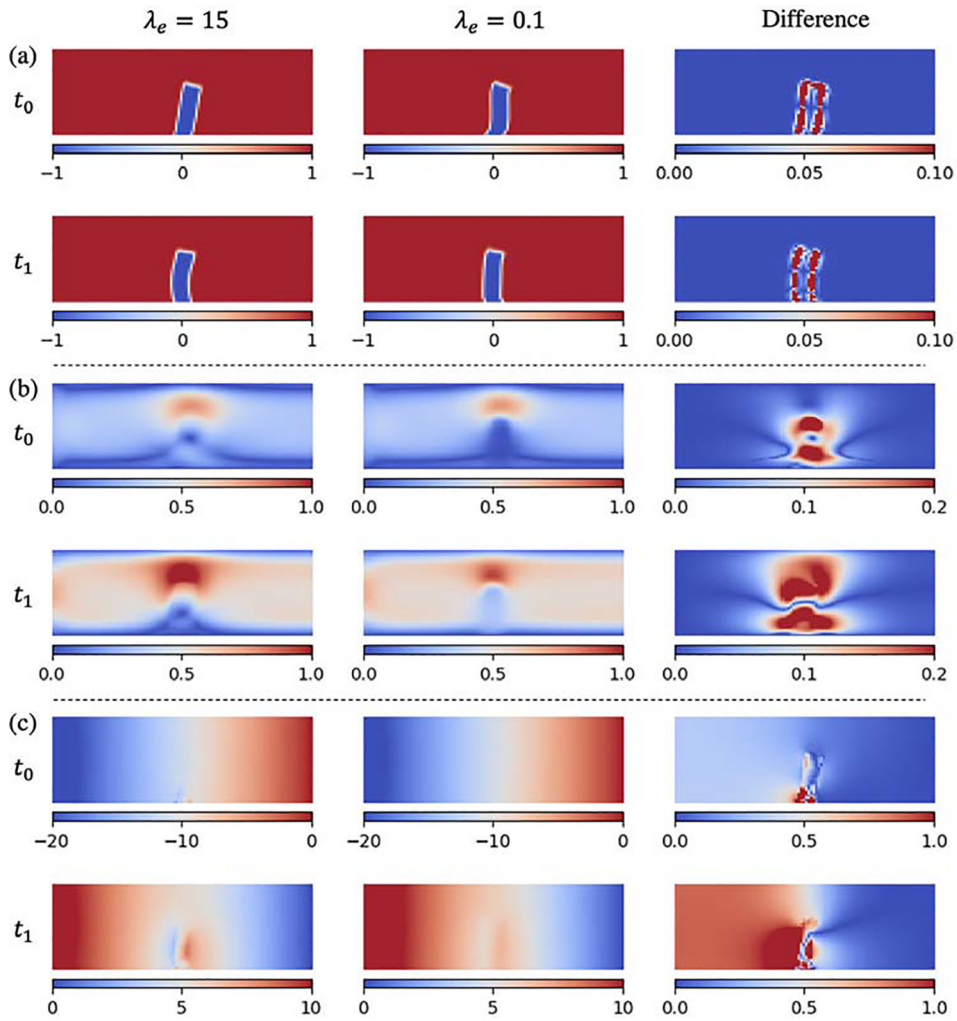

Figure 16: 2D flow past a viscoelastic biofilm for λ_e = 15 and 0.1.

The first two lines show the phase field different at t_0 = 0.44 and t_1 = 0.86. The middle two lines and the last two lines show the comparison of velocity and pressure at t_0 and t_1. The last column presents the absolute difference between fields data when λ_e = 15 and 0.1.

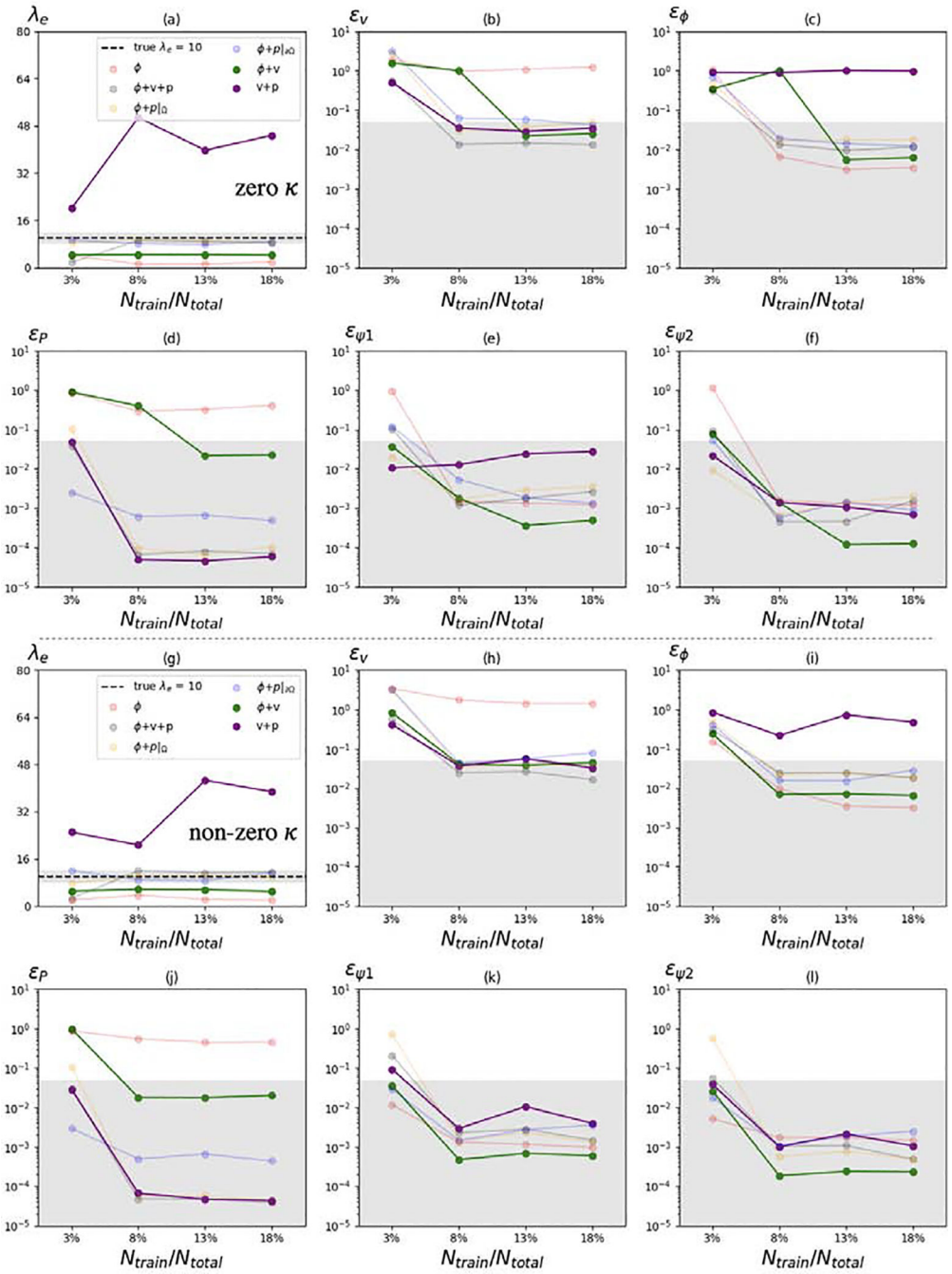

Figure 17: Results for the biofilm case with additional results.

We train the PINN model with p+u and ϕ+u as comparisons, and we plot the inference results and errors on the top of Fig. 13 with opaque lines indicating the new results. The shaded areas indicate that the error is lower than 5%.

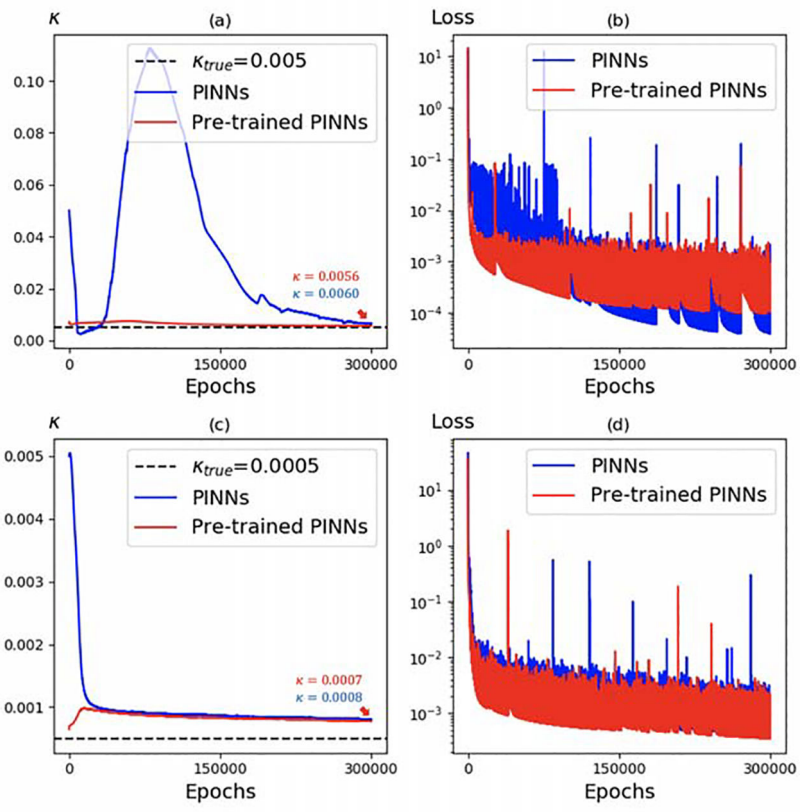

Figure 18: Effect of using a pre-trained model on the inference of κ = 0.005 and 0.0005.

(a, c) compare the history of inferred κ from the model with and without pre-training versus epochs. (b, d) shows the training loss versus epochs for each model. The pre-trained model is adopted as the weights and biases for κ = 0.5 at last epochs.

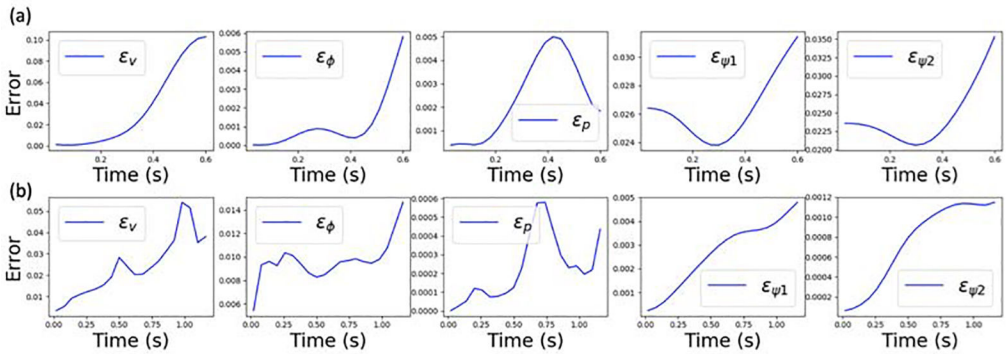

Figure 19:
Relative L2 error over the full time window for the (a) cavity and (b) biofilm example.

Table 1:

Summary of the mean relative L_2 error for the thrombus in a cavity over half and full time window.

Training points in the cavity problem are sampled from $t \in [0.03, 0.63]$. The half window relative errors are defined as the errors from $t \in [0.03, 0.33]$, whereas the full window relative errors are defined as the errors from $t \in [0.03, 0.63]$

	ϵ_v	ϵ_ϕ	ϵ_p	ϵ_{ψ_1}	ϵ_{ψ_2}
Full	3.511×10^{-2}	1.157×10^{-3}	2.391×10^{-3}	2.636×10^{-2}	2.450×10^{-2}
Half	4.494×10^{-3}	4.129×10^{-4}	1.057×10^{-3}	2.516×10^{-2}	2.236×10^{-2}

Table 2:

Summary of the mean relative L_2 error for the biofilm problem over half and full time window.

Training points in the biofilm problem are sampled from $t \in [0.02, 1.16]$. The half window relative errors are defined as the errors from $t \in [0.02, 0.56]$, whereas the full window relative errors are defined as the errors from $t \in [0.02, 1.16]$.

	ϵ_v	ϵ_ϕ	ϵ_p	ϵ_{ψ_1}	ϵ_{ψ_2}
Full	2.396×10^{-2}	9.700×10^{-3}	2.260×10^{-4}	2.665×10^{-3}	7.453×10^{-4}
Half	1.417×10^{-2}	8.893×10^{-3}	9.090×10^{-5}	1.490×10^{-3}	4.016×10^{-4}